Appl. Phys. B 53, 170–179 (1991)

Applied Physics B Photophysics and Laser Chemistry

Photoacoustic Measurements of Lorentz Broadening in CO_2 Between 25° C and 450° C*

M. Hammerich[1], L. Vildrik-Sørensen[1], H. de Vries[2], and J. Henningsen[3]

[1] Physics Laboratory, H.C. Ørsted Institute, Universitetsparken 5, DK-2100 Copenhagen Ø, Denmark
[2] Department of Physics, University of Nijmegen, Toernooiveld, NL-6525 ED Nijmegen, The Netherlands
[3] Danish Institute of Fundamental Metrology, Bldg. 307, Lundtoftevej 100, DK-2800 Lyngby, Denmark

Received 30 March 1991/Accepted 22 May 1991

Abstract. A variable temperature photoacoustic cell has been constructed and tested by studying the interplay of CO_2, H_2O, and NH_3 in synthetic smoke. Saturation effects for CO_2 and NH_3 have been modeled and compared with experiments, and results are obtained for the vibrational relaxation rate associated with NH_3–H_2O collisions. The cell has been used for studying the temperature dependence of self-broadening and N_2 broadening of CO_2 lines. The temperature dependence of the scattering rate is well described by a T^{-n} law with $n=0.77$ in both cases. This result agrees with previous results obtained by tunable diode laser spectroscopy, but disagrees with results obtained by indirect methods.

PACS: 33.70Jg, 34.50Ez, 7.65G

The study of molecular absorption lines as a function of temperature is of interest from several points of view. The infrared vibration-rotation lines provide unique fingerprints of individual molecules, and may be used for monitoring purposes. The strength of the absorption can be used for quantitative measurements of molecular concentrations, and the shape and width of the lines provide information about the local environments, such as temperature and particle density. Thus, to fully extract all possible information from the line, it is necessary to know how parameters such as the line strength, and the collision cross section for various partners, depend on temperature.

Applications which rely on such information are found in the realm of basic research, as well as in applied research. An example of the former is the study of planetary atmospheres, including that of the planet Earth, or conditions in interstellar molecular clouds, while industrial applications include the monitoring of molecules in exhaust from combustion processes.

The most commonly employed method for studying temperature effects in infrared spectroscopy, is that of linear absorption. This works well for relatively strong lines, but for weak lines the absorption is seen as a small change in a large transmitted signal, and it is viewed on the background of the noise spectrum of the unattenuated radiation source. The signal can be improved by using the long path length offered by multipass configurations such as the White cell. However, then mirror absorption may become troublesome, and the relatively large cell volume will limit the response time of the system.

From many points of view, photoacoustics represent an attractive alternative way of measuring infrared absorption. The technique was introduced more than 100 years ago by Bell [1], Tyndall [2] and Röntgen [3], but remained of little practical interest until the advent of lasers gave rise to a surge of applications [4–6]. In this technique, the radiation source is modulated at an audio frequency. The energy absorbed by the molecule is lost via inelastic collisions and converted to heat, and eventually the absorption will give rise to a pressure modulation, which can be picked up by a microphone. Thus, unlike linear absorption, it is a zero-background technique, and a combination of high sensitivity and fast time response can be achieved by using a small cell volume.

In the context of high temperature, however, the use of photoacoustics is hampered by the requirement of having a microphone tightly coupled to the cell volume, since commercially available microphones hardly survive 100° C. One way of separating the microphone from the high temperature interaction region is by using a Helmholtz resonator consisting of two cavities, coupled by a long duct. Using this technique, Bechtold et al. [7] studied phase transitions in solids up to 1050 K, and a theoretical analysis of such resonators is given by Pelzl et al. [8]. The

* Supported by the Danish Science Research Council under grant no. 11-7777, and by FLS-airloq A/S

purpose of the present paper is to present a novel cell design which allows for measurements between −100° C and 450° C, to study the cell performance under conditions relevant to monitoring of smoke stack emission, and to demonstrate the applicability of the cell in basic research by studying collision broadening parameters in CO_2 as a function of temperature.

In Sect. 1, we describe the construction of the cell, as well as the experimental details in general. Section 2 discusses the various factors that determine the response to different molecules under a wide range of conditions, and Sect. 3 is concerned with a calculation of the saturation behavior under conditions relevant to our experiments. Section 4 gives the results of measurements aimed at verifying the cell performance as a function of pressure and temperature. Since one of the aims of the present work is to extend to higher temperature the monitoring of NH_3 in power plant emission [9], particular emphasis is given to the study of CO_2 and NH_3 in a background of gases normally present in smoke stacks. Section 5 contains the result of collision broadening measurements on pure CO_2, as well as on CO_2 in a background of N_2, over the temperature range 25–450° C. Finally, Sect. 6 contains a summary and conclusions.

1. Experiment

1.1 Cell Construction

The photoacoustic cell is shown in Fig. 1. It consists of a 200 mm long tube of SS304 stainless steel, with inner diameter 10 mm, terminated in one end by a chromium backed gold mirror on a quartz substrate, and in the other end by a NaCl Brewster window. Thus, unlike the frequently used open organ pipe resonator [10], this cell has pressure maxima at the ends, and a node at the center. Two microphones (Knowles EK3024) are mounted back to back in a side branch, close to the Brewster window, and two heat coils are used for heating the mirror end of the resonator to a maximum temperature of 450° C, while the microphone end is maintained at room temperature. The temperature is measured by chromel-alumel thermocouples close to the mirror, and close to the exit port, and between sample entrance and exit, the cell temperature is constant to within ±5° C. Although we have only performed detailed measurrements above room temperature, the cell has also been operated without problems at dry ice temperature.

The sample gas enters the cell through a steel nozzle at the mirror end, and is pumped out after traversing about one third of the cell length. The diameter of the nozzle is chosen such that with a pressure of 1 bar at the high pressure side, a flow on the order of 50 mlSTP/min results in an operating pressure in the cell of about 25 mbar. At the same time, dry air enters at the microphone end of the cell and is pumped out at the common pump port. This serves the dual purpose of protecting the microphone against the hot sample gas, and avoiding excitation of the resonator at the microphone end.

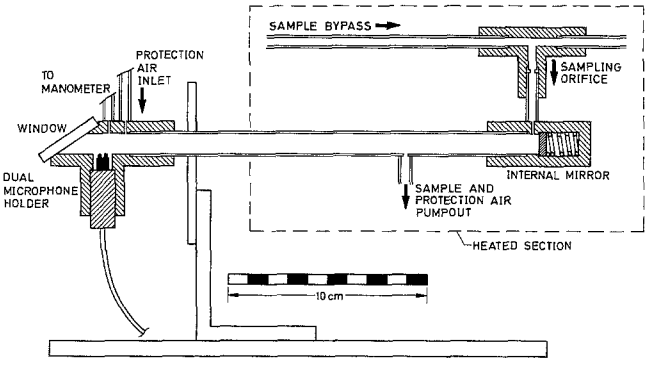

Fig. 1. Photoacoustic cell design

1.2 Gas Supply

Sample gas is supplied to the heated bypass line from a system of three flow controllers, followed by a heater and a heated mixing chamber. One of the flow ontrollers provides a premixed combination of 76% N_2, 8% O_2, and 16% CO_2, which in the following will be denoted "synthetic smoke". The second controller provides 0.1% NH_3 in N_2, while the third is used for supplying H_2O. This is done by bubbling N_2 through water which can be temperature stabilized anywhere between room temperature and 100° C. The synthetic smoke controller has a nominal maximum flow rate of 500 mlSTP/min, whereas the remaining two controllers are rated 50 mlSTP/min. The pressure in the cell was monitored by an absolute pressure gauge with 0.1 mbar resolution.

1.3 Laser and Optical Path

The CO_2 laser uses a 240 mm pyrex waveguide with 2.9 mm inner diameter, and the total resonator length is 356 mm, yielding a tuning range of 400 MHz, taking into account 4% frequency pulling. The design is similar to that described in [11], and the laser is optimized for single line and single mode operation according to the guidelines given in [12]. The laser is pulsed at a repetition rate of 785 Hz. When tuned to the 9R30 line, it provides up to 220 mW of average power in pulses with a half width of 10 μs, and a peak power of 25 W at the line center, and 15 W at the edge of the tuning range, i.e. at ±200 MHz.

The layout of the experiment is shown in Fig. 2. The beam is focused to a beam waist radius of 1.0 mm, located

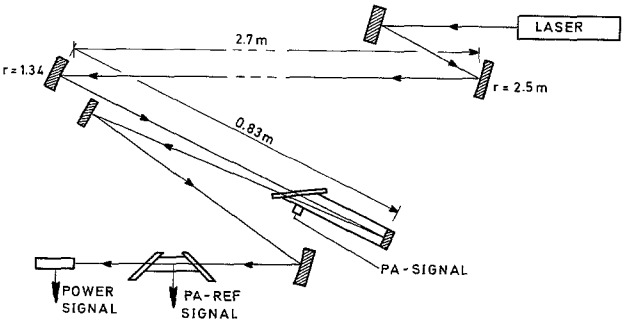

Fig. 2. Experimental layout

at the mirror at the rear end of the cell. After leaving the cell, the beam passes through a short reference photoacoustic cell containing CO_2 at a pressure of about 10 mbar, before it reaches the power monitor.

1.4 Data Collection and Data Analysis

Under normal operating conditions, the pressure in the photoacoustic cell is maintained at 25 mbar, at a flow of about 50 mlSTP/min. At this pressure, the width of the absorption lines is significantly smaller than the tuning range of the laser, and well-resolved line profiles can be distinguished from CO_2 at the line center, and from the $sR(5,0)$ NH_3 line situated at an offset of -190 MHz relative to the CO_2 line center. None of the other gases used in the mixture give any detectable response in $9R30$.

A measurement consists of a computer controlled scan of the laser over three free spectral ranges. Utilizing the CO_2 line center position as recorded by the reference cell, together with the sharp kinks in the power profile at the edge of the tuning range, a second-order polynomial is generated, which transforms the nonlinear piezo displacement axis into a linear frequency axis. The photoacoustic signal, demodulated with a dual lock-in amplifier, is normalized with respect to the laser power, and the result is fitted to a sum of two Voigt profiles with complex amplitudes, using the known line center position, and a Doppler width calculated for the measured temperature in the cell.

2. Responsivity

When considering the responsivity for a given molecule, it is convenient to distinguish between that part which is determined by the acoustical properties of the cell, and that which depends on the specific properties of the molecule under consideration. In the commonly encountered case, where the molecule is present at a small concentration in a background of buffer gas of essentially constant composition, this distinction is unambiguous. This is not the case if the molecule is present at such large concentration that it influences the thermodynamic properties of the gas in the cell. Nevertheless, it is still convenient to maintain the distinction, which now relates to the cell properties on one hand, and to the strength of the driving field on the other hand.

The molecular properties that determine the excitation strength, are quantified through the small signal absorption coefficient and the saturation parameter, and we shall denote their contribution to the overall responsivity as R_m. For a given resonator, characterized by its resonance frequency f_0 and quality factor Q, the responsivity depends on the efficiency with which the acoustic energy created by the molecular absorption, is coupled into the relevant resonator mode. This efficiency has a temporal and a spatial aspect. We quantify the temporal aspect through the factor R_t, describing the frequency dependent response of the resonator

$$R_t \propto \left\{\left[1-\left(\frac{f}{f_0}\right)^2\right]^2+\left(\frac{f}{Qf_0}\right)^2\right\}^{-1/2}. \tag{1}$$

The spatial aspect is more difficult to quantify. It is determined by the combined spatial overlap between the laser beam, the distribution of active molecules, and the resonator mode, and we describe it through a factor R_s. Following these considerations, we thus write the overall responsivity R as the product

$$R=R_m R_t R_s. \tag{2}$$

2.1 Resonator Characteristics

At a given acoustic frequency, the responsivity R_t depends on the resonance frequency and the Q-value of the acoustical resonator, and these again both depend on gas composition, and on pressure and temperature in the cell.

The normal acoustical modes of a cylindrical resonator are given by Kreuzer in [Ref. 4, Chap. 1]. When operating in the lowest order longitudinal resonance, the important losses occur in boundary layers at the walls, and they are characterized by the lengths

$$d_v=(2\mu/\varrho\omega)^{1/2} \tag{3}$$

and

$$d_h=(2K/\varrho\omega C_p)^{1/2} \tag{4}$$

which represent the thickness of the viscous and the thermal boundary layer respectively. Neglecting volume losses, the Q-value of the resonator is given by

$$Q=\frac{r}{d_v+(\gamma-1)d_h}, \tag{5}$$

where r is the radius of the resonator, μ is the coefficient of viscosity, ω is the acoustic angular frequency, K is the heat conductivity of the gas, and $\gamma=C_p/C_v$, where C_p and C_v denote the specific heat capacity at constant pressure and constant volume respectively. For an ideal gas, the coefficient of viscosity μ is given by

$$\mu=\frac{1}{3}\sqrt{\frac{8kmT}{\pi\sigma}},$$

where k is the Boltzmann constant, m the molecular mass, σ the collision cross section, and T the absolute temperature. The thermal conductivity K, is related to μ through

$$\frac{K}{\mu}=\frac{C_v}{m} \tag{6}$$

and the density ϱ is given by

$$\varrho=\frac{mP}{kT}, \tag{7}$$

where P is the static pressure. Inserting in the expression for Q, we find the pressure and temperature scaling

$$Q\propto P^{1/2}T^{-3/4}. \tag{8}$$

For fixed geometry, the resonance frequency f_0 of the resonator is proportional to the velocity of sound s, which is given by

$$s=\frac{1}{\sqrt{\kappa\varrho}}, \tag{9}$$

where κ is the adiabatic compressibility, given by

$$\kappa = \frac{1}{\gamma P}. \tag{10}$$

The result is that the resonance frequency is independent of pressure, but scales as

$$f_0 = \frac{s}{2L} \propto T^{1/2} m^{-1/2}, \tag{11}$$

where L is the length of the resonator.

The scaling laws, as derived above, will apply to a resonator with uniform temperature and pressure. However, under normal operating conditions different parts of our cell may be at different temperature, and deviations can be expected. Inserting numerical values appropriate to dry N_2 at 25° C and 25 mbar, we arrive at a theoretical Q-value of 4.0 for $r = 0.5$ cm. This might seem low, but it should be noted that the motivation for using a resonant cell is to enable transmission of the acoustic signal from the sample region to the microphone region, rather than to obtain a resonant enhancement of the sensitivity. In addition, a high Q-value would lead to technical complications in temperature scans, owing to the need for tracking the resonance.

2.2 Molecular Characteristics

The excitation strength for a given molecule depends on the transfer of energy from the laser field to vibration and rotation in the molecule, as well as on the subsequent conversion of internal molecular energy into translational energy of the gas as a whole.

a) The absorption coefficient. The vibrational excitation is instantaneous, and the strength is determined by the absorption coefficient. This again depends on the transition dipole moment of the transition under consideration, and through the lineshape function and the partition function it depends on pressure and temperature in the gas. The presence of other molecules in the gas mixture will influence the absorption coefficient through the collisional broadening, since the cross section for collisions depends on the collision partner. This effect must also be taken into account at high concentration, if the cross section for self-collisions is significantly different from the cross section for collisions with the molecules of the background gas.

b) Saturation. The transfer of vibrational energy into translational energy is characterized by the cross section for vibrational deexcitation, either directly through V–T relaxation, or through intermediate vibrational levels, involving V–V relaxation. The V–T relaxation rate is generally much slower than the rotational R–R relaxation, which determines the collisional broadening of the absorption line. A consequence of the slow V–T relaxation is that the photoacoustic response may be limited by saturation. If this is the case, it is important to note that the cross section for V–T relaxation may be vastly different for different collision partners. Thus, even a small concentration of molecules with a large cross section, such as H_2O, may significantly reduce the saturation, and hence change the responsivity of the system. In Sect. 3, we shall consider this problem in detail, focusing on the saturation behaviour of NH_3 and CO_2.

c) Kinetic cooling. In mixtures of CO_2 and N_2, the near degeneracy between the first excited level of the asymmetric stretch of CO_2, and the first vibrationally excited state of N_2, leads to a rapid transfer of vibrational energy from CO_2 to N_2 through resonant collisions. After the passage of the laser pulse, fast vibrational relaxation among the (0n°0) levels quickly restores thermal equilibrium in this vibrational ladder. This implies a transfer of vibrational energy into the (02°0) state, and the required energy is supplied by the translational degree of freedom. Since the absorbed energy can reside for a long time in the very long-lived excited N_2 level, the net result is a transient cooling of the gas, and this effect has been described in the literature as kinetic cooling [13]. Under short pulse excitation, this leads to a considerable phase change relative to the photoacoustic signal from absorption in a molecule which does not exhibit kinetic cooling. This phase contrast can be used as a means for discriminating between absorption from CO_2 and other molecules in a background containing N_2 [9].

For dry N_2 at 25 mbar, the lifetime of the vibrationally excited N_2 states is very long as compared to the acoustical period. The absorbed energy will then lead to an increase in the average temperature of the gas, and the only signal detected at the modulation frequency will be that related to the kinetic cooling. This situation changes if the gas contains molecules which, via collisions with N_2, can speed up the relaxation back to the vibrational ground state. In particular H_2O is very efficient in this respect, owing to its large permanent dipole moment, and we consequently expect a change both in the responsivity and the phase of the CO_2 signal, if water is added to the gas mixture [14].

3. Saturation

For cw laser radiation, saturation effects are important whenever the rate of stimulated absorption is comparable to or exceeds the collisionally induced relaxation rate of the upper level. In the case of a pulsed laser, however, also the pulse width is of importance. If the pulse width is long as compared to the relaxation time, the saturation behavior will be essentially similar to the cw case. If, on the other hand, the pulse width is much smaller than the relaxation time, relaxation during the pulse can be neglected. Saturation is then determined by the ratio between the total number of molecules excited during the pulse, and the number of molecules available for excitation.

3.1 Model

In this section, we calculate the saturation intensity for pulsed radiation with arbitrary pulse width. A typical

pulse consists of a gain switched spike, followed by a main pulse. The half width Δ of the main pulse is roughly inversely proportional to the operating pressure of the laser, and at our normal pressure of 160 mbar, it is about 10 μs. In the following, we shall neglect the spike, which contains about 2% of the energy, and approximate the main pulse by the analytic expression

$$P(t)=P(0)\exp\left[-\left(\frac{t}{\Delta}\right)^2\ln 2\right]. \tag{12}$$

For the molecules considered in this work, the R–R relaxation rate, which is responsible for the collision broadening of the absorption lines, is of the order of 2 MHz/mbar, corresponding to a relaxation rate of $\sim 5\times 10^7\,s^{-1}$ at 25 mbar. This is more than two orders of magnitude larger than the other characteristic times of the problem, and we shall therefore consider R–R relaxation to be instantaneous. We assume homogeneous broadening and model the molecule as a two level system, described by the following equations

$$\frac{dN_1}{dt}=W(t)gN_0(t)-\frac{N_1(t)}{\tau}, \tag{13}$$

$$N_1(t)+N_0(t)=N. \tag{14}$$

Here, N_i denotes the total density of molecules in the i-th vibrational manifold, $W(t)$ is the rate of stimulated absorption, g is the statistical weight of the lower state rotational level, and τ is the V–T relaxation rate. $W(t)$ is proportional to the laser intensity $I(t)$, and is given by

$$W(t)=\frac{\sigma}{h\nu}I(t), \tag{15}$$

where σ is the cross section for stimulated absorption.

It is convenient to introduce dimensionless units, and we therefore write

$$t=\theta\Delta, \tag{16}$$

$$\tau=k\Delta, \tag{17}$$

$$I(t)=I(0)i(\theta), \tag{18}$$

$$i(\theta)=\exp(-\theta^2\ln 2), \tag{19}$$

$$\frac{\sigma g I(0)}{h\nu}=\frac{A}{\Delta}, \tag{20}$$

$$n_i(\theta)=\frac{N_i(\theta)}{N} \tag{21}$$

resulting in the equation

$$\frac{dn_1}{d\theta}=Ai(\theta)-Ai(\theta)\frac{1}{k}n_1(\theta) \tag{22}$$

with the boundary condition $n_1(0)=0$. Having solved this rate equation, the absorbed energy per pulse U, is given by

$$U=\frac{Nh\nu}{k}\int_0^\infty n_1(\theta)d\theta. \tag{23}$$

Parameters used in the numerical calculations are given in the Appendix. The results of the calculations are shown in Fig. 3, where the relative absorbed energy per pulse, normalized to its limiting value in the small signal limit, is plotted for different values of the dimensionless intensity A, as a function of the dimensionless relaxation time k. Two limiting cases can be dealt with analytically. In the limit of $k\gg 1$, we can neglect relaxation during the pulse, and we get

$$U=Nh\nu\left[1-\exp\left(-\frac{A}{2}\sqrt{\frac{\pi}{\ln 2}}\right)\right]. \tag{24}$$

Note that in this case, the saturation becomes independent of the relaxation time. For the other limiting case of $k\ll 1$, we get a quasi cw situation, where the population of the upper level follows the applied intensity. In this case, we arrive at

$$U=Nh\nu\int_0^\infty\frac{A\exp(-\theta^2\ln 2)}{1+Ak\exp(-\theta^2\ln 2)}d\theta. \tag{25}$$

Defining the dimensionless saturation intensity A_s as that value of A, for which the relative absorbed energy takes half the small signal value, we find the relation between A_s and k given in Fig. 4. The graph is constructed by drawing a horizontal line through $U/U_0=0.5$ in Fig. 3 to intersection with the curve for a given A, and identifying the corresponding value of k. In the limit $k\ll 1$, we find $A_s=1.53/k$, while in the opposite limit of $k\gg 1$, $A_s=1.50$ is independent of k.

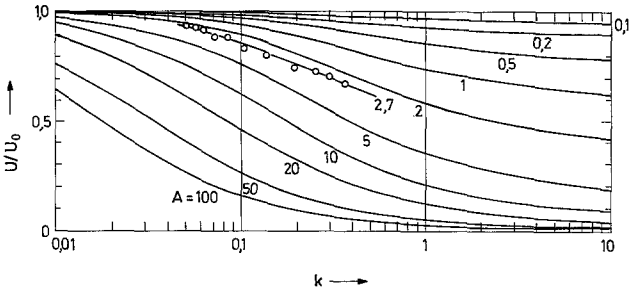

Fig. 3. Calculated change in responsivity to NH_3 due to saturation. The parameter A is the normalized laser intensity, defined in (21), the variable k is the normalized V–T relaxation time, in units of the laser pulse half width, U is the energy absorbed per pulse, and U_0 is its limiting small signal value. Experimental changes caused by the addition of H_2O are plotted into the graph

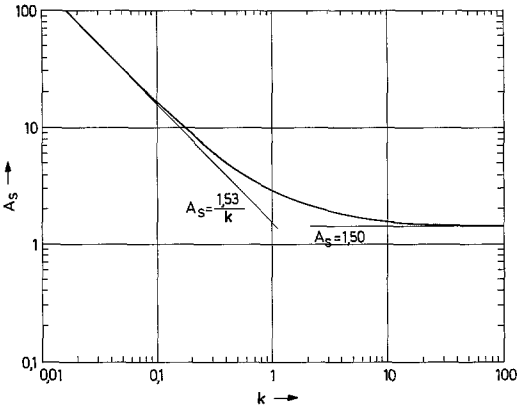

Fig. 4. Calculated saturation parameter A_s as a function of normalized V–T relaxation time k

Under our operating conditions of 25 mbar and 400 K, for dry NH_3 in N_2, we are at $k \sim 0.6$ and $A \sim 2$, and from Fig. 3, we see that this corresponds to substantial saturation. For CO_2 on the other hand, we are at $k \sim 100$ and $A \sim 0.1$. In this limit, $A_s = 1.5$, and since $A \ll A_s$, saturation is unimportant. Note that the absence of saturation for CO_2 is a consequence of the pulsed conditions. Under cw conditions, the saturation parameter is given by the product Ak, and the CO_2 transition would in fact be strongly saturated.

4. Cell Performance

4.1 Frequency Response

The frequency-dependent response R_t of (2) has been studied by using a single pulse excitation source. The transient microphone response was recorded as a function of temperature and pressure by a digital storage oscilloscope (Fig. 5a). Subsequently, the data were Fourier transformed to yield the response in the frequency domain (Fig. 5b). The resonance frequency f_0 was determined from the transform, whereas the Q-value was determined from an exponential fit to a subset of the local response extrema in the time domain (Fig. 5a). In the analysis, the excitation was considered as a delta function in time. To check the validity of this assumption, measurements were carried out on different gas mixtures, including 200 ppm of NH_3 in a background of N_2 and 10% of H_2O, where the V–T relaxation is known to be much faster than the pulse period. However, essentially similar results were obtained when using 16% CO_2 in dry N_2, and the data presented below are based on the latter gas mixture. Note that throughout the following, the temperature will refer to the interaction region of the cell.

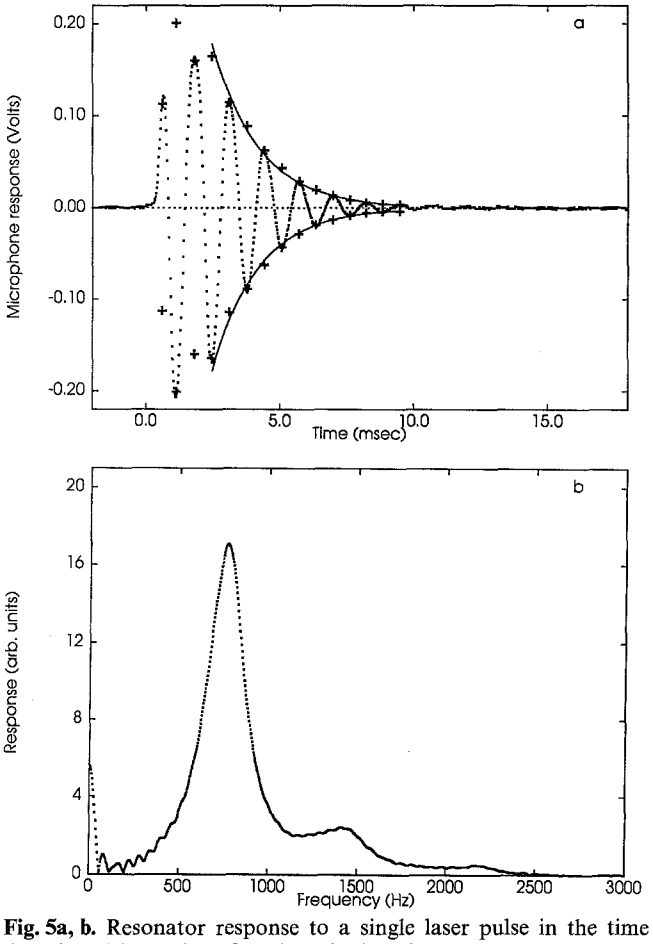

Fig. 5a, b. Resonator response to a single laser pulse in the time domain, with envelope function obtained by exponential fit (−) to response extrema (+) **(a)**, and corresponding response in the frequence domain **(b)**

4.2 Pressure and Temperature Dependence

When the sample end of the cell is heated from room temperature to 400° C at constant pressure between 10 and 100 mbar, the resonance frequency increases by about 10%. Qualitatively, an increase is expected according to (12), and we shall not attempt to quantify the consequences of the extremely nonuniform temperature distribution. For constant temperature, f_0 increases by about 5% as the pressure is changed from 10 to 100 mbar. Thus, to a good approximation, f_0 is independent of pressure as suggested in Sect. 2.1.

At 25 mbar and 25° C we measure a Q of 3.5, in surprisingly good agreement with the calculated value of 4, considering the rather large perturbations of the ideal resonator geometry. However, upon increasing the pressure from 10 to 100 mbar, the Q-value increases by only about 20%, whereas the $P^{1/2}$ scaling predicted by kinetic gas theory would correspond to more than a factor of 3. At present we have no explanation for this.

In order to obtain an estimate for the third factor R_s of the overall responsivity, we have measured the overall response R at 25 mbar for 16% CO_2 in dry N_2, at a fixed pulse frequency of 785 Hz, over the temperature interval 25 to 450° C. The temperature dependence of R_t is determined from the measured temperature dependence of f_0 and Q, in conjunction with (1), and in Fig. 6, the measured values of R/R_t are compared with the calculated absorption coefficient, representing R_m. The calculation was performed using the parameters given in the Appendix, and scaled into agreement with the data points at 25° C. We find that as the temperature increases, there is a growing discrepancy between the measurements and the calculations, and we interpret this as being caused by a 50% decrease in R_s over the temperature range considered. An explanation for the temperature dependence of R_s may be found in the fact that different parts of the cell are at different temperature. To an acoustic wave propagating in the resonator, the transition region at the center will be seen as a change in wave impedance, and the energy will be partly reflected. Thus, with increasing temperature difference, it is conceivable that it gets progressively more difficult for the acoustic energy to be transmitted from the interaction region to the microphone region. Also, with increasing temperature of the interaction region, the tendency for active molecules to diffuse into the microphone region will increase, leading to reduced excitation efficiency.

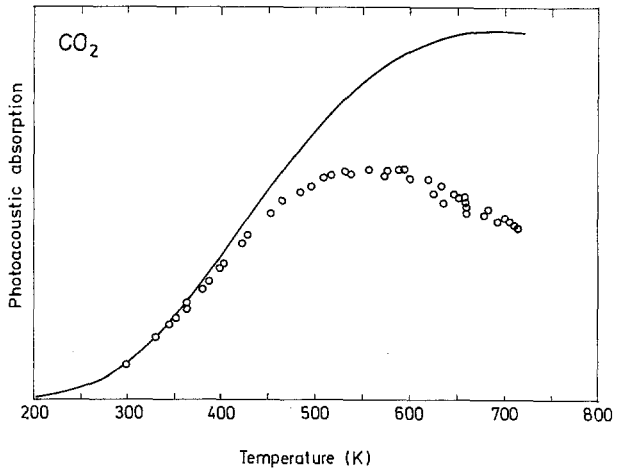

Fig. 6. Photoacoustic response for 16% CO_2 in dry N_2, as a function of temperature at 25 mbar. The response is expressed as $R = R_m R_t R_s$, where R_m is the absorption coefficient, R_t the temporal, and R_s the spatial variation of the photoacoustic cell responsivity. The solid curve is the calculated R_m, and the circles are measured values of R/R_t. The discrepancy accounts for the temperature dependence of R_s

4.3 Effect of H_2O on the Responsivity for CO_2

Experimentally, it is found that the addition of H_2O to dry synthetic smoke leads to an increased response to CO_2, and that the phase of the signal is advanced. Figure 7a shows the responsivity for CO_2, scaled to 16%, with and without 100 ppm NH_3, for water concentrations in the range 0–9%. The responsivity increases fast with the water concentration, until it reaches a maximum at about 1%, and from then on it decreases slowly. Following this change in responsivity is a monotonic increase in the phase of about 110°, as shown in Fig. 7b.

The change in responsivity is primarily due to a change in excitation efficiency of the resonator, caused by the changing delay between the rapid kinetic cooling and the delayed heating of the gas. Qualitatively, we expect the excitation efficiency to reach a maximum when the delay between the two signals corresponds roughly to one half modulation period, so that they will excite the resonator with the same phase. Superimposed on this, we have the effect of changes in the resonance frequency, caused by the gradual change in gas composition. However, owing to the rather low Q-value, the contribution of the latter effect will hardly exceed the statistical uncertainty of the measurements.

4.4 Effect of H_2O on the Responsivity for NH_3

As suggested in Sect. 2.2b, the addition of small amounts of water to the gas mixture is expected to affect the responsivity to NH_3. Figure 8 shows the measured NH_3 response, scaled to 100 ppm, for a mixture of synthetic smoke and approximately 100 ppm NH_3, as a function of the water concentration in the range 0–9%. We find that the decrease in saturation leads to a monotonic increase in responsivity, while there is no measurable change in the phase.

An estimate for the V–T relaxation rate for NH_3–H_2O collisions may be obtained by recourse to the results of Sect. 3. Using as adjustable parameters the normalized relaxation rate k in the dry limit, the normalized relaxation rate for H_2O–NH_3 collisions, and the normalized intensity, A, we have fitted the results of Fig. 8 into the collection of curves in Fig. 3. The data points entered in Fig. 3 correspond to $A = 2.7$ and $k = 0.37$. Using $\Delta = 10\,\mu s$, this value of k corresponds to a scattering rate of

$$\gamma_{dry} = 1.08 \times 10^4\,s^{-1}\,mbar^{-1}.$$

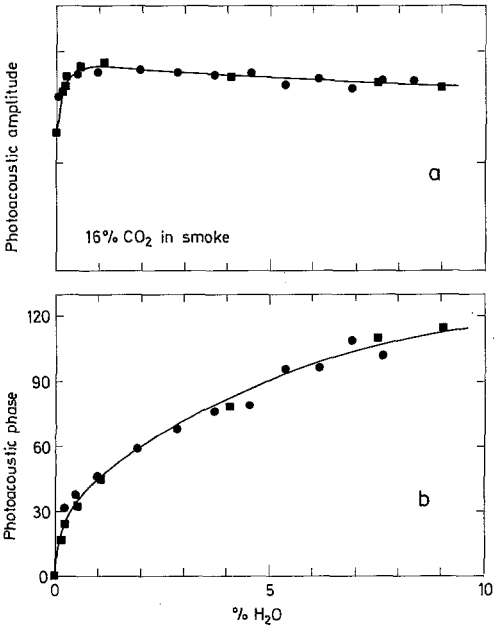

Fig. 7a, b. Photoacoustic amplitude in arbitrary units **(a)** and phase **(b)** as a function of H_2O content for 16% CO_2 in synthetic smoke. Different symbols refer to data taken on different days

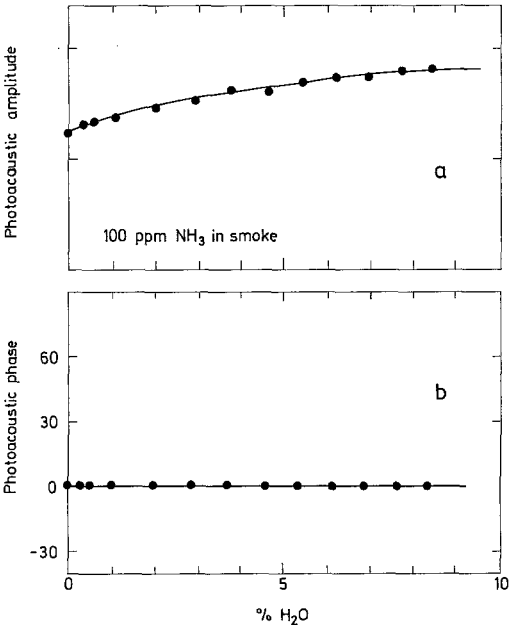

Fig. 8a, b. Photoacoustic amplitude in arbitrary units **(a)** and phase **(b)** as a function of H_2O content for 100 ppm NH_3 in synthetic smoke

This value is slightly larger than the value

$$\gamma_{N_2} = 0.77 \times 10^4 \, s^{-1} \, mbar^{-1}$$

found by Danagher and Reid [17] for NH_3 in dry N_2, and we attribute this to the presence of 16% CO_2 in the background gas.

The scattering rate for H_2O–NH_3 collisions is found as

$$\gamma_{H_2O} = 0.98 \times 10^6 \, s^{-1} \, mbar^{-1}$$

which is slightly larger than the value

$$\gamma_{NH_3} = 0.86 \times 10^6 \, s^{-1} \, mbar^{-1}$$

found by Danagher and Reid for NH_3 self-collisions.

From the measured pulse profile, an average power of 65 mW at the NH_3 line center, and a beam waist radius of 1 mm, we find a peak intensity of 150 W/cm^2, averaged over the Gaussian spot. This corresponds to $A = 2.1$, in quite fair agreement with the value $A = 2.7$ producing the best fit.

5. Collision Broadening

One type of investigation for which our cell is well suited, is the study of collision broadening as a function of temperature. If molecules are considered as hard spheres with a temperature independent cross section, the Lorentz contribution to the linewidth at constant pressure will scale as $T^{-1/2}$. This result has rarely emerged from experiments, and it is therefore customary to model the temperature dependence of the Lorentz width γ as

$$\gamma(T) = \gamma(T_0)\left(\frac{T_0}{T}\right)^n,$$

where n may differ significantly from $\frac{1}{2}$. One indication of the increasing interest in the temperature dependence of γ is the fact that information on n is included in the most recent versions of the data bases GEISA [19] and AFGL [20, 21].

Varanasi [22] has published a review of measurements of n for a number of molecules of relevance to the study of planetary atmospheres. Although he focuses on data obtained at the low temperatures typical of such atmospheres, high temperature data are also included. In particular for CO_2, high temperature data are important in connection with the atmosphere of Venus, which offers an example of a runaway greenhouse effect. Varanasi quotes eight works dealing with self-broadening and N_2 broadening of CO_2, and one striking feature is the large scatter of the data. To some extent this may reflect real variations in n for different lines, but quite likely it also reflects a statistical uncertainty, which is particularly large in those cases where only a 100° temperature interval is used for deducing n, or where indirect methods are used, which do not involve the entire line profile.

We have measured the Lorentz contribution to the linewidth for the line 9R30 in the 00°1→02°0 band for 100% CO_2 as well as for 10% CO_2 in N_2, over the temperature range 300–720 K. At six different temperatures, the line was recorded as a function of pressure over the interval 10–60 mbar, and fitted to a Voigt profile, using a calculated value for the Doppler width. For 10% CO_2 in N_2, the absorption in the cell is insignificant, and the photoacoustic signal was normalized with respect to the laser power level after the beam exits the cell. For 100% CO_2, however, at the highest temperatures, the absorption burns a sizeable hole in the power profile, and the photoacoustic signal was therefore normalized with respect to the laser power level at the rear end of the cell, given by $\sqrt{P_{in} \cdot P_{out}}$, where P_{in} and P_{out} is the power entering and leaving the cell. In this case, it was possible to deduce the Lorentz width from the emerging power profile, and hence to check the results obtained by photoacoustics. The two sets of data were consistent, but the statistical quality of the photoacoustic data is far superior.

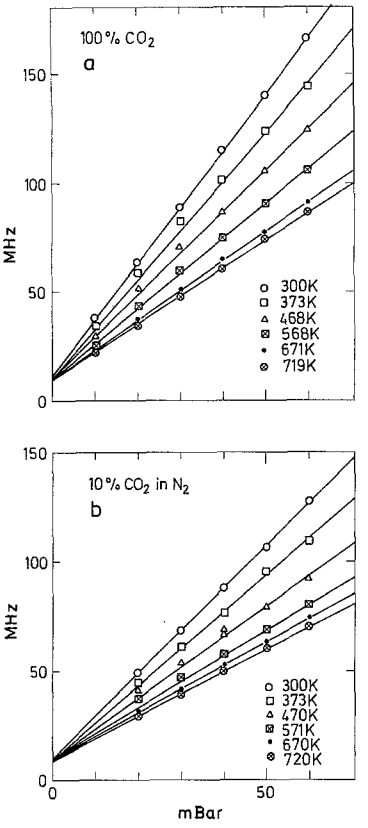

Fig. 9a, b. Lorentz width (HWHM) as a function of pressure and temperature for 100% CO_2 **(a)** and for 10% CO_2 in N_2 **(b)**

The results for the pressure dependence of the Lorentz width is shown in Fig. 9. In all cases, we get straight lines with a common zero intercept of 10 MHz, corresponding to the spectral width of the laser. The temperature dependence is analyzed in the double logarithmic plot in Fig. 10. In both cases, we find that the presumed power law dependence is well satisfied, with an n of 0.77 ± 0.05. At 300 K, the ratio between the two broadening rates is 0.76. The self-broadening rate is directly measured as 2.58 MHz/mbar, and this leads to an N_2 broadening rate of 1.89 MHz/mbar, corresponding to a ratio of 0.73 between the rates for N_2 broadening and self-broadening. This result is in perfect agreement with the result given by [23], and cited in numerous papers on the CO_2 laser.

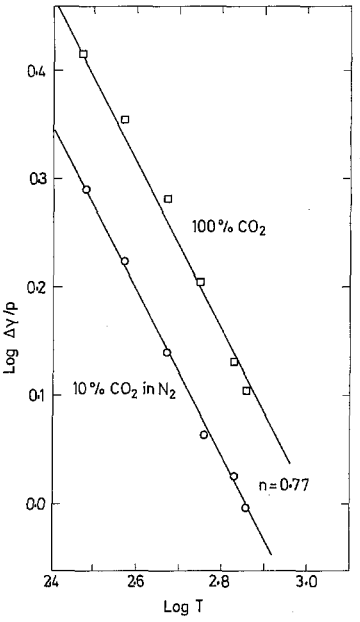

Fig. 10. Determination of the power law exponent for the temperature dependence of the Lorentz width

6. Conclusion

A low-Q resonant photoacoustic cell is described, which enables operation in the temperature range $-100°$ C to $+450°$ C. Over this temperature interval, changes in the acoustical properties of the resonator will cause variations of up to 50% in responsivity, when operating the radiation source at fixed modulation frequency.

A prime objective has been to study the interplay between NH_3 and other components of the emission from power plants employing denox installations. For this purpose, the saturation behavior of NH_3 and CO_2 under conditions of pulsed excitation have been modeled, and the results compared with experiments. For NH_3 it is found that saturation is important, and that the degree of saturation is significantly changed by the addition of H_2O in quantities typical of those present in smoke. This leads to a change in responsivity, and calls for attention to the water content, if the cell is used for quantitative monitoring.

For CO_2 saturation is found to be unimportant, but the addition of water leads to a drastic modification of the kinetic cooling, which is a characteristic of the CO_2–N_2 system. The change in amplitude and phase of the photoacoustic response is studied as a function of the water content, and it is shown that the phase changes monotonically over the range 0–9%. This allows for a determination of the water content, and hence enables evaluation of the correction factor for the NH_3 responsivity.

The experiments are performed under conditions which allow monitoring of the absorption line profiles over a 400 MHz interval. This has been used for studying the temperature dependence of the Lorentz broadening of the $R30$ line of the $00°1 \rightarrow 02°0$ band in CO_2 over the temperature interval 25–450° C. The result for 10% CO_2 in N_2 is in very good agreement with the supposed T^{-n} power law, with the exponent $n=0.77$. For 100% CO_2, the data seem to indicate a slight deviation from the power law, although a best straight line fit in Fig. 10 leads to the same result for n. This value for the power exponent is in excellent agreement with a previous measurement on the P18 line of the same band, performed by tunable diode laser spectroscopy [24], and yielding $n=0.764$. However, it disagrees markedly from numerous results obtained by indirect methods [22], and this emphasizes the need for using the entire line profile for deducing the Lorentz broadening.

Appendix: Numerical Values

In this appendix we summarize the parameters used for numerical evaluation of the saturation intensity and the absorption coefficient for NH_3 and CO_2.

The cross section for stimulated absorption σ is given by

$$\sigma(\nu)=\frac{\pi\nu\langle\cos^2\theta\rangle\mu^2}{\varepsilon c\hbar}g_V(\nu). \tag{26}$$

μ is the magnitude of the transition dipole moment, and is taken as 0.81×10^{-30} Cm for NH_3 and 1.12×10^{-31} Cm for CO_2. The direction cosine matrix element $\langle\cos\theta^2\rangle$ can be found in [15] and is 0.182 for $sR(5,0)$ in NH_3, and 0.169 for $9R30$ in CO_2. At the line center, the Voigt lineshape function $g_V(\nu)$ is given by

$$g_V(0)=\frac{1}{\Delta\nu_D}\sqrt{\frac{\ln 2}{\pi}}\,\mathrm{Re}\{w(iy)\}, \tag{27}$$

where

$$y=\frac{\Delta\nu_L}{\Delta\nu_D}\sqrt{\ln 2} \tag{28}$$

$$w(z)=\exp(-z^2)\,\mathrm{erfc}(-iz) \tag{29}$$

and $\mathrm{erfc}(z)$ is the complementary error function. $\Delta\nu_L$ is the Lorentz width, and $\Delta\nu_D$ the Doppler width, both HWHM. The Doppler width is assumed to scale as $T^{1/2}$. For the Lorentz broadening, no precise measurements exist for the temperature dependence in the case of NH_3. We use the value 2.66 MHz/mbar at 300 K, and assume a hard sphere model, leading to a $T^{-1/2}$ scaling. For CO_2, we use the results of Sect. 4, and assume $T^{-0.77}$ scaling.

The statistical weight for a particular rotation-inversion state in NH_3 is given by [15]

$$f_{J,K}=\frac{S(I,K)}{4I^2+4I+1}\,\frac{2J+1}{Z(T)}\exp-\frac{BJ(J+1)+(C-B)K^2}{kT}, \tag{30}$$

where the nuclear spin quantum number $I=\frac{1}{2}$, $S(I,K)=4I^2+4I+3$ if K is a multiple of 3, and $S(I,K)=4I^2+4I$ if this is not the case, and where B and C are the rotational constants. For the partition function we use the symmetric top expression

$$Z(T)=\sqrt{\frac{\pi(kT)^3}{B^2C}}. \tag{31}$$

For the lower level of the $sR(5,0)$ transition, this yields

$$f_{5,0}=0.0774\left(\frac{300}{T}\right)^{3/2}\exp\left(-\frac{429}{T}\right). \tag{32}$$

For CO_2, we use the partition function as calculated by [16]. Over the temperature range 300–500 K, the analytic expression

$$Z(T)=291\left(\frac{T}{300}\right)^{3/2} \tag{33}$$

is correct to within about 3%, but for accurate calculations over extended temperature intervals, the exact partition function must be used. With the analytic approximation, the statistical weight for lower level of the $9R30$ transition is

$$g=0.210\left(\frac{300}{T}\right)^{1.39}\exp\left(-\frac{523}{T}\right). \tag{34}$$

For pure CO_2, the bottleneck determining saturation is the V–V transfer from (001) to (03°0). Taylor and Bitterman [18] have surveyed vibrational relaxation data for the CO_2–N_2 laser system, and from their paper we find a rate constant of $40\,s^{-1}\,mbar^{-1}$ at 400 K. For NH_3, the V–T relaxation rate has been determined for the ν_2 band by Danagher and Reid [17]. They find for collisions with N_2 a rate constant of $7.7\times10^3\,s^{-1}\,mbar^{-1}$, and for self-collisions $8.6\times10^5\,s^{-1}\,mbar^{-1}$. Danagher and Reid performed their study at room temperature, and since no information is available on the temperature dependence, we use the room-temperature result.

References

1. A.G. Bell: Phil. Mag. **11**, 510 (1881)
2. J. Tyndall: Proc. R. Soc. Lond. **31**, 307 (1881)
3. W.C. Röntgen: Phil. Mag. **11**, 308 (1881)
4. Y.H. Pao (Ed.): *Optoacoustic Spectroscopy and Detection* (Academic, New York 1977)
5. V.P. Zharov, V.S. Lethokov: *Laser Optoacoustic Spectroscopy* (Springer, Berlin, Heidelberg 1986)
6. P. Hess (Ed.): *Photoacoustic, Photothermal and Photochemical Processes in Gases*, Topics Appl. Phys. **46** (Springer, Berlin, Heidelberg 1989)
7. P.S. Bechtold, M. Campagna, T. Schober: Solid State Commun. **36**, 225 (1980)
8. J. Pelzl, R. Klein, O. Nordhaus: Appl. Opt. **21**, 94–99 (1982)
9. A. Olafsson, M. Hammerich, J. Bülow, J. Henningsen: Appl. Phys. B **49**, 91–97 (1989)
10. E. Krikhman, S. Shtrikman, M. Slatkine: J. Opt. Soc. Am. **68**, 1257 (1978)
11. F. Tang, J. Henningsen: Appl. Phys. B **44**. 93–98 (1987)
12. J. Henningsen, M. Hammerich, A. Olafsson: Appl. Phys. B **51**, 272–284 (1990)
13. F.G. Gebhardt, D.C. Smith: Appl. Phys. Lett. **20**, 129–132 (1971)
14. P.W. Huber, A. Kantrowitz: J. Chem. Phys. **15**, 275 (1947)
15. C.H. Townes, A.L. Schawlow: *Microwave Spectroscopy* (McGraw-Hill, New York 1955)
16. L.D. Gray, J.E. Selvidge: J. Quantum Spectrosc. Radiat. Transfer **5**, 291–301 (1965)
17. D.J. Danagher, J. Reid: J. Chem. Phys. **86**, 5449–5455 (1987)
18. R.L. Taylor, S. Bitterman: Rev. Mod. Phys. **41**, 26–47 (1969)
19. N. Husson et al.: Ann. Geophys. **4**, 185 (1986)
20. L.S. Rothman et al.: Appl. Opt. **22**, 2247–2256 (1983)
21. L.S. Rothman et al.: Appl. Opt. **26**, 4058 (1986)
22. P. Varanasi: J. Quantum Spectrosc. Radiat. Transfer **39**, 13–25 (1988)
23. A. van Leberghe, S. Arillier, C.J. Bordé: IEEE J. QE-**14**, 481 (1978)
24. R.S. Eng, A.W. Mantz: J. Molec. Spectrosc. **74**, 331 (1979)